Influence of Artificial Aging on Corrosion of Abraded Al-Zn-Mg-Cu Alloys

Shan-Shan Wang [1,*], D. Huber [2], J.D. Poplawsky [3], and G.S. Frankel [1]

[1] *Fontana Corrosion Center, The Ohio State University, Columbus, OH 43210, USA*

[2] *Center for Electron Microscopy and Analysis, The Ohio State University, Columbus, OH 43210, USA*

[3] *Center for Nanophase Materials Sciences, Oak Ridge National Laboratory, Oak Ridge, TN 37831, USA*

[*] Corresponding author. E-mail: wang.3608@osu.edu.

Abstract

Surface abrasion has been shown to create altered surface layers (ASLs) that are hundreds of nm thick on all types of Al alloys. Such ASLs have lower corrosion resistance than the underlying substrate of Al-Zn-Mg-Cu alloys. Here, we demonstrate how heat treatments affect the ASL microstructure on abraded Al-Zn-Mg-Cu alloys using transmission electron microscopy and atom probe tomography, and also how the corrosion properties change using electrochemical polarization. High temperature treatments on the abraded bulk samples enhance η phase precipitation in the ASL, leading to a decreased Zn content in the ASL solid solution, which ennobles the ASL breakdown potential.

Keywords: Aluminum alloy; Subsurface; Microstructure; Polarization; Transmission electron microscopy; Atom probe tomography.

1. Introduction

Industrial processing such as rolling, machining, and grinding can create near-surface deformed layers on Al alloys [1–8]. For example, mechanical grinding is often conducted on a finishing line before applying paint in the automobile industry. Heat treatment simulating the paint baking process enhances precipitation in the deformed layers, resulting in a lower content of noble elements in the matrix solid solution of the deformed layers than in the underlying substrate of Al-Mg-Si and Al-Mn alloys, which increases the susceptibility to filiform corrosion on painted samples due to the dissolution of the near-surface deformation layer under the paint [1,2].

Surface abrasion with grinding paper and polishing are commonly used to provide fresh and low-roughness surfaces. However, such processes introduce heavy shear deformation to the surface and create near-surface deformed layers with depth ranging from a few nm to hundreds of nm from the extreme surface on a wide range of substrates including glass [9], Cu [10], stainless steel [11], and all types of Al alloys [12–16]. To differentiate the deformed layers created by industrial processing, we have referred to the deformed layers produced by surface abrasion as altered surface layer (ASL) [15]. Such ASLs on metal substrates affect measured polarization curves and the associated corrosion phenomena [11–16]. For instance, the ASL on abraded/polished AA7XXX-T6 is more susceptible to corrosion than the underlying bulk and preferentially dissolves, resulting in a sharp current increase at low potentials in the potentiodynamic polarization curve measured in NaCl solution [13,15]. Depending on the conditions, the current can reach a peak and then decrease, and then rapidly increase again so that the curve exhibits two breakdown potentials, the first associated with the ASL dissolution and the second from the initiation of stable pitting in the underlying substrate. In contrast, only pitting corrosion occurs on AA7XXX-T73 without the ASL dissolution [12,15]. The ASL on AA2024 is

slightly less susceptible to corrosion than the underlying substrate [14]. Clearly the ASLs on different substrates have different corrosion properties.

We have recently shown that the ASL microstructure on AA7055 is extremely unstable at room temperature, and its evolution depends on sample dimensions [17,18]. Various new phases that are not commonly present in AA7XXX, such as pure Zn, Al_2Cu and AlCu, precipitate and grow in the ASL during natural aging of abraded bulk samples as well as transmission electron microscopy (TEM) foils that were taken from the abraded surfaces [18]. The acceleration of the microstructural changes in the deformed subsurface in certain TEM foils is greater than that in bulk samples, due to enhanced surface diffusion of the thin TEM sample geometry [18]. Long-term natural aging of abraded AA7055-T6 ennobles the ASL and results in an increase in the first breakdown potential measured by potentiodynamic polarization in NaCl solution [19]. However, the effects of artificial aging on the ASL microstructure and corrosion on AA7XXX-T6 have not been reported previously. The high strength Al-Zn-Mg-Cu alloys are susceptible to corrosion and are often painted to provide corrosion resistance in service. It is therefore of interest to know how heat treatments simulating paint baking affect the corrosion properties of the abrasion-induced ASL on Al-Zn-Mg-Cu alloys.

Previous work has characterized the ASL microstructure evolution during natural aging of AA7055-T6 TEM specimens over a period of 2 to 60 months and unusual Al_2Cu phases were found to grow in the ASL [19]. However, the very early-stage ASL microstructure on abraded AA7055-T6 was not reported. In this work, the abrasion process, focused ion beam (FIB) sectioning and TEM characterization were performed in a single day to capture the ASL microstructure on a freshly abraded AA7055-T6 bulk sample. Atom probe tomography (APT) was used to analyze the solute distributions in the ASL. TEM and APT analysis were also performed on the abraded and heated bulk samples to study how temperature affects the ASL microstructure.

Anodic polarization curves were measured to evaluate the corrosion properties. The relationship between heat treatments, the ASL microstructure and polarization behavior of Al-Zn-Mg-Cu alloys was discussed.

2. Experimental

AA7055 (Al-7.76Zn-1.94Mg-2.35Cu-0.12Zr, wt%) and AA7075 (Al-5.5Zn-2.5Mg-1.5Cu, wt%) rolled plates with T6 peak-aging treatments were studied. The alloy samples were ground using SiC grinding paper from 240 to 1200 grit under ethanol to remove the original rolled/machined surface and produce fresh surfaces. Any ASL observed on these samples would have resulted from the grinding process. APT and TEM specimens were prepared from the abraded surfaces using focused ion beam (FIB). High-angle annular dark-field (HAADF) imaging and EDS maps were performed in scanning TEM mode. Two needle-shaped APT specimens were fabricated from the abraded AA7055-T6 surface using FIB through standard liftout and sharpening procedures with a 2 kV final polishing step [20]. SEM images of the liftout location and the needle-shaped specimen were giving in Supplementary Figure 1. The FIB and APT measurement procedures are the same as those reported previously [18]. The top ~50 nm of the APT dataset was removed prior to analysis to prevent the presence of ion beam damage from sample preparation.

Potentiodynamic polarization testing was conducted on the abraded samples with different conditions in aerated and deaerated 3.5 wt% NaCl solution using a potentiostat. N_2 gas was used to deaerate the solution. The alloy sample, Pt electrode and saturated calomel electrode (SCE) served as working electrode, counter electrode, and reference electrode, respectively. After stabilizing at the open circuit potential (OCP) for 0.5 h, the applied potential was scanned in a positive direction from the OCP at a scan rate of 0.1 mV/s. The polarization testing was performed

on two or three samples for each condition. The polarization curves shown below are representative of the set.

3. Results and Discussion

A TEM specimen was extracted from the freshly abraded AA7055-T6 surface using FIB, immediately followed by TEM observation, and the HAADF images and EDS maps of the subsurface microstructure are shown in Figures 1 and 2. The original subgain boundaries, indicated by green arrows, were deformed toward the abrasion direction and mostly did not extend into the region above the dashed line. In this region with depth of around 200 nm from the extreme surface, newly formed subgrain boundaries (indicated by pink arrows) were observed. The high magnification HAADF image and EDS maps in Figure 2 show that large Mg_xZn_y and Al_xCu_y particles precipitated at the subgrain boundaries in the ASL. As expected, Ga originating from the FIB process was enriched within the subgrain boundaries and Mg_xZn_y phases. The main precipitates in the underlying substrate are η′ ($Mg(Zn,Cu,Al)_2$) phases. However, some η′ precipitates in the ASL close to the extreme surface disappeared, and η′ precipitates in the bottom part of the ASL were deformed towards the abrasion direction. The same phenomena were observed in another TEM specimen that was extracted from the freshly abraded AA7055-T6 sample (Supplementary Figure 2), indicating that the observations are reproducible.

The freshly abraded ASL microstructure on AA7055-T6 was slightly different than the previous ASL observation that was conducted as early as 2 months after surface abrasion, in which well-defined subgrains were observed in the entire ASL, most of the fine η′ precipitates decomposed and only one type of new phase, Al_2Cu (θ), precipitated at the subgrain boundaries [19]. The reason for the difference is that the ASL microstructure can change rapidly at room temperature, and its

evolution is affected by the sample dimensions (bulk or TEM specimen) [17,18]. The Al-Zn-Mg-Cu alloy microstructure is typically stable at room temperature, and it requires high temperature treatment for phase transformations to occur. However, surface abrasion introduces shear deformation to the Al alloy surface and creates a high density of defects such as dislocations and excess vacancies. The residual shear stress in the ASL can stimulate dislocation motion and accelerate phase transformation kinetics by solute transport through defects [17,18]. Therefore, the times at which FIB sectioning and TEM examination were conducted relative to surface abrasion are critical in determining the deformed subsurface microstructure.

The ASL on the freshly abraded AA7055-T6 sample is also different than that on the freshly abraded AA7055-T73 sample [18], in which original η′/η precipitates and grain boundaries were rotated and deformed along the abrasion direction but without new phase formation or decomposition of original η′/η precipitates [18]. The reason for this difference is related to differences in the bulk microstructures of these two samples. AA7055-T6 has smaller semi-coherent η′ precipitates, whereas AA7055-T73 has larger semi-coherent η′ and incoherent η precipitates. When the surface is subjected to the shear deformation, it is easier for the dislocations to shear through the smaller η′ precipitates in AA7055-T6 than η′ and η precipitates in AA7055-T73. Similar phase decomposition has been observed in Al-Cu alloys and pearlitic steel during heavy plastic deformation at room temperature, such as fragmentation and decomposition of θ precipitates in an Al-Cu alloy during the equal channel angular pressing [21], dissolution of Cu-Mg co-clusters near a crack tip in an Al-Cu-Mg alloy due to cyclic deformation [22], and cementite decomposition of cementite in a heavily cold drawn pearlitic steel [23]. As described previously [18], once η′ precipitates decompose, some solutes are transported by defects such as dislocations

and excess vacancies to the newly formed subgrain boundaries, at which θ and Mg_xZn_y phases can precipitate.

The ASL microstructure was not uniform, so two needle-shaped APT specimens were fabricated at random positions from the abraded surface. The tips of the APT needles started ~ 50 nm away from the extreme surface, and they were oriented such that the long axis was perpendicular to the surface. APT analysis of one needle-shaped specimen in Figure 3 confirms the absence of fine η′ precipitates at the top of the APT needle where the ASL is located, and the presence of η′ precipitates with a composition of 36 at% Zn, 24 at% Mg, 2.3 at% Cu and balance Al in the underlying substrate (Figure 3b). The one-dimensional concentration profile in Figure 3c shows that, high Zn and Cu contents were present in the ASL solid solution. Further analysis of the Zn- and Cu-rich region at the top of the needle shows that, this region contained almost 40 at% Zn and 10 at% Cu (Figure 3d), which likely resulted from the decomposition of fine η′ precipitates. In previous studies [13,15], EDS line scans showed a slight Zn enrichment at subgrains boundaries in the ASL, which was believed to be responsible for the corrosion-susceptible ASLs on AA7XXX-T6. However, the APT analysis in the current study leads to the new observation of a higher Zn content in the ASL matrix than in the underlying bulk. This may lead to the observed ASL susceptibility to corrosion. The Ga and Zr maps were given in Supplementary Figure 3. Ga implantation is common in APT specimen preparation for Al alloys.

Figure 4 shows APT analysis of a second needle-shaped specimen from the same abraded AA7055-T6 surface. There were a few larger η′/η precipitates at the middle of the needle and a high density of smaller η′ precipitates at the top and bottom of the needle. TEM results show that the ASL microstructure is not uniform, and so there are variations in precipitate number/volume density across the APT needle. The bottom of the needle should be located at the substrate below

the ASL. The region close to the extreme surface, in which the η′ precipitates decomposed, was not fully captured in this APT needle. Proximity histograms were used to create composition profiles for the precipitates at these three locations (Figures 4c-e and Supplementary Figure 4). The smaller precipitate compositions are likely underestimated due to artificial mixing of matrix and precipitate ions as a result of APT aberrations at the precipitate/matrix interfaces [24].

The freshly abraded AA7055-T6 sample was heated at 110 °C for 24 h, immediately followed by FIB sectioning and TEM observation. A high density of larger precipitates was observed in the ASL than in the underlying bulk substrate (Figure 5). The EDS maps in Figure 6 show that most precipitates contain high concentrations of Mg and Zn, which are likely η phases. An Al_xCu_y phase was also observed in the heat treated ASL. Recent work has shown that aging of a freshly abraded AA7055-T73 bulk specimen at 50 °C for 1 h accelerates the formation of subgrains and Al_2Cu phases in the entire ASL [18], which is significantly different than the ASL microstructure on the abraded and 110 °C/24 h heated bulk sample. Heat treatments at different temperatures promote different phase transformations. The temperature 110 °C is close to the typical temperature for T6 peak aging, 120 °C, at which η′ precipitates form. An aging treatment at 110 °C after surface abrasion considerably enhanced the precipitation of η phases in the ASL, resulting in less Mg, Zn and Cu solutes in the ASL solid solution. These solute elements are known to have different effects on the breakdown potential of Al alloys; Zn solute in the Al matrix decreases the breakdown potential, whereas Cu solute increases it, and Mg has little effect [25,26]. The solute redistributions should affect the corrosion properties of the ASL.

Two needle-shaped APT specimens were also fabricated at random positions from the abraded and artificially aged (110 °C/24 h) sample surface, and the APT analyses were given in Figure 7 and in Supplementary Figure 5. There was no Zn-rich region in the needles. The composition of

precipitates was 39.2 at% Zn, 26.5 at% Mg, 3.4 at% Cu and balance Al. APT specimens only represent very small regions, whereas TEM specimens represent larger areas. TEM examination in Figure 5 has clearly shown the effects of post heat treatment on the ASL microstructure. Enhanced η phase precipitation was observed in the heated ASL, leading to less solute contents in the ASL, which might affect the ASL breakdown potential.

To test this assumption, potentiodynamic polarization testing was conducted on bulk abraded and heat-treated samples in deaerated 3.5wt% NaCl solution. The AA7055-T6 bulk samples were first abraded to 1200 grit finish, followed by heating at 50 °C, 80 °C or 110 °C for different periods of time. Polarization testing was conducted in deaerated solution to decrease the OCP and separate it from the first breakdown potential. Therefore, the value of the first breakdown potential is not affected by an oxygen reduction reaction, but mainly by the Al anodic reaction. The full polarization curves are given in Supplementary Figure 6. To clarify the differences in the first breakdown potentials, only the regions of the polarization curves near the breakdown potentials are shown in Figure 8. All the samples studied here experienced passive regions at low potentials before they reached the first breakdown potential at which the current started to increase rapidly by several orders of magnitude (indicated by the arrows). The passive current densities for all the samples were similar and within a range of $2 \times 10^{-7} \sim 6 \times 10^{-7}$. Heat treatments had minor effects on passive current densities. The first breakdown potentials were caused by the active dissolution of the ASL, leaving a uniform corrosion product on the surface after polarization, similar to what was observed previously for susceptible ASLs on Al-Zn-Mg-Cu alloys [13,15]. As described previously [13,15], the ASL was more active to corrosion than the underlying substrate so that the ASL was dissolved as a layer at lower potentials while the underlying matrix was not attacked. The ASL that extended under the O-ring in the polarization testing setup was also attacked, leaving

a crevice between the O-ring and the underlying substrate. As the upward scan continued, crevice corrosion of the underlying substrate occurred, resulting in the second potential at which the current increased rapidly again. Pitting corrosion on the boldly exposed underlying substrate occurred at higher potentials.

Here we focus on the effects of post heat treatment on the first breakdown potential caused by ASL dissolution. With increasing aging temperature and time, the first breakdown potential increased to less negative values, indicating that the heat treatment following surface abrasion ennobled the ASL. Post heat treatments at 50 °C only increased the ASL breakdown potential by small values, within 20 mV (Figure 8a). Post heat treatment at 80 °C for only 1 h increased the ASL breakdown potential to a value similar to that for the heat treatment at 50 °C for 24 h, –750 mV SCE (Figures 8a and b). By prolonging the aging time at 80 °C to 24 h, the value of the ASL breakdown potential was significantly increased to –715 mV SCE (Figure 8b). At the higher aging temperature of 110 °C, the value of the ASL breakdown potential was around –730 mV SCE and –710 mV SCE after aging for 1 and 12 h, respectively (Figure 8c). However, with continued aging at 110 °C to 24 h, the ASL breakdown potential slightly decreased to –730 mV SCE (Figure 8c). Nevertheless, post heat treatments ennobled the ASL breakdown potentials. This is consistent with the assumption that the phase precipitation in the ASL during aging treatments resulted in lower contents of solutes in the ASL solid solution, which in turn affected the ASL corrosion properties. Zn and Cu solutes have opposite and competitive effects on the breakdown potential of the Al matrix [25,26]. The effect of the decreased Zn content in the ASL solid solution should be dominant, making the ASLs less active to corrosion. The negative effect of the decreased Cu content started to be evident at the later stage of high-temperature aging, as indicated by a slight decrease in breakdown potential with extended aging time from 12 h to 24 h at 110 °C. However,

even when the ASL breakdown potential was significantly increased to –710 mV SCE for the sample that was abraded and aged at 110 °C for 12 h (Figure 8c), a current peak was observed, and a uniform corrosion product was still observed on the sample surface after polarization. This suggests that, in this condition, the ASL was still more susceptible to corrosion than the underlying substrate.

Polarization testing was also performed on the abraded and heated AA7075-T6 samples in air-exposed and stagnant 3.5 wt% NaCl solution. ASLs on AA7075 and their impacts on corrosion were first observed by Zhao and Frankel [12,13]. Figure 9a shows that, similar to AA7055, heat treatments after surface abrasion increased the ASL breakdown potentials of AA7075. In particular, for the AA7075 sample that was abraded and aged at 110 °C for 24 h, only one breakdown potential occurred. After polarization, only pitting corrosion was observed at the localized sites, with no uniform corrosion product observed on the surface (Figure 9c). This suggests that the ASL did not preferentially dissolve as a layer. Instead, the ASL breakdown potential was very close to that of the underlying substrate, so only pitting corrosion occurred. This is different from AA7055 exhibiting ASL dissolution even after high-temperature aging treatments, which may be due to the different alloy compositions of the two alloys. AA7075 has lower Zn and Cu contents than AA7055. It is reasonably assumed that post high-temperature heat treatments also enhance η phase precipitation in the ASL on AA7075, resulting in less Zn and Cu content in the ASL solid solution. The decreased Cu content lowers the breakdown potential. Such a negative effect might not be less evident in AA7075, due to the lower content of Cu in this alloy. Therefore, after high-temperature heat treatment, the ASL on AA7075 did not fully dissolve as occurred on AA7055.

It is possible that the passivating oxide film thickened during heat treatment in an oven exposed to air. To check if the ennoblement of the ASL breakdown potential resulted from a passivation

film growth or the ASL microstructural changes, a freshly abraded sample was encapsulated in a glass tube that was evacuated and then filled with inert Ar gas, and then heat treated at 110 °C for 24 h (Figure 9b). This encapsulated sample exhibited a similar polarization curve as the sample without encapsulation, indicating that the ennoblement of the ASL breakdown potential was caused by the ASL microstructural changes and not passive film growth. The heated sample was ground again with a 1200 grit finish, and the measured polarization curve was similar to the freshly abraded sample, because the active ASL was created again by re-abrasion and dissolution during polarization, leaving a uniform corrosion product on the corroded surface (Figure 9d).

In summary, the details of the ASL microstructure and its evolution play a critical role in the corrosion properties of abraded Al alloys. The deformed subsurface microstructure can change rapidly at room temperature in both bulk sample and TEM specimens [18]. It is therefore critical to characterize the deformed microstructure in a timely manner. APT analysis provides new insight into solute redistributions in the ASL, revealing a higher Zn content in solid solution of the ASL than in the underlying bulk of AA7055-T6. High temperature treatments after abrasion reduced the Zn matrix content in the ASL by enhancing η phase precipitation, which increased the ASL breakdown potentials. Heat treatment in an inert environment resulted in the same polarization curve, indicating that the ennoblement of the ASL was caused by ASL microstructural changes during heat treatment and not passive film thickening.

4. Conclusions

The subsurface microstructures on abraded AA7055-T6, and their effects on corrosion were studied. There following conclusions can be drawn:

1. During or immediately after surface abrasion, subgrains already formed in the ASL, some fine η′ precipitates decomposed, and new Mg_xZn_y and Al_xCu_y phases precipitated at the subgrain boundaries.
2. APT analysis shows that the very early-stage ASL contains a higher Zn content in solid solution than in the underlying bulk. This resulted from the decomposition of fine η′ precipitates and may be the main reason for the ASL susceptibility to corrosion.
3. Heat treatments after abrasion at temperatures as low as 50 °C increased the ASL breakdown potentials of Al-Zn-Mg-Cu alloys. In particular, treatment at the high temperature 110 °C for 24 h significantly promoted the precipitation of coarse η precipitates in the ASL, leading to less Zn content in the solid solution of the ASL than in the underlying bulk, which considerably ennobled the ASL. The ASL breakdown potentials increased with increasing the post aging temperature (50 °C, 80 °C and 110 °C) and time.
4. Despite the ennoblement of the AA7055 ASL breakdown through post heat treatments, the ASL was still more susceptible to corrosion than the underlying bulk, resulting in the ASL dissolution during polarization. In contrast, only pitting corrosion occurred in abraded AA7075-T6 after a high-temperature aging treatment.

Data availability

The data that support the findings of this study are available from the corresponding author upon reasonable request.

Acknowledgements

FIB and TEM were performed at Center for Electron Microscopy and Analysis at The Ohio State University. APT was conducted at ORNL's Center for Nanophase Materials Sciences (CNMS), which is a U.S. DOE Office of Science User Facility. We acknowledge Prof. Liang Zhen and Prof. Jian-Tang Jiang for providing AA7055 materials. This research was not supported by any grants from funding agencies in the public, commercial, or not-for-profit sectors.

References

[1] A. Afseth, J.H. Nordlien, G.M. Scamans, K. Nisancioglu, Influence of heat treatment and surface conditioning on filiform corrosion of aluminium alloys AA3005 and AA5754, Corrosion Science. 43 (2001) 2359–2377. https://doi.org/10.1016/S0010-938X(01)00019-1.

[2] Y. Liu, X. Zhou, G.E. Thompson, T. Hashimoto, G.M. Scamans, A. Afseth, Precipitation in an AA6111 aluminium alloy and cosmetic corrosion, Acta Materialia. 55 (2007) 353–360. https://doi.org/10.1016/j.actamat.2006.08.025.

[3] X. Zhou, Y. Liu, G.E. Thompson, G.M. Scamans, P. Skeldon, J.A. Hunter, Near-surface deformed layers on rolled aluminum alloys, Metallurgical and Materials Transactions A. 42 (2011) 1373–1385. https://doi.org/10.1007/s11661-010-0538-2.

[4] G.M. Scamans, M.F. Frolish, W.M. Rainforth, Z. Zhou, Y. Liu, X. Zhouc, G.E. Thompsonc, The ubiquitous beilby layer on aluminium surfaces, Surface and Interface Analysis. 42 (2010) 175–179. https://doi.org/10.1002/sia.3204.

[5] A. Afseth, J.H. Nordlien, G.M. Scamans, K. Nisancioglu, Effect of heat treatment on filiform corrosion of aluminium alloy AA3005, Corrosion Science. 43 (2001) 2093–2109. https://doi.org/10.1016/S0010-938X(01)00014-2.

[6] H. Leth-Olsen, J.H. Nordlien, K. Nisancioglu, Filiform corrosion of aluminium sheet. III. Microstructure of reactive surfaces, Corrosion Science. 40 (1998) 2051–2063. https://doi.org/10.1016/S0010-938X(98)00094-8.

[7] J. Wang, X. Zhou, G.E. Thompson, J.A. Hunter, Y. Yuan, Microstructure Evolution in the Near-Surface Region During Homogenization of a Twin-Roll Cast AlFeMnSi Alloy, Metallurgical and Materials Transactions A. 47 (2016) 4268–4275. https://doi.org/10.1007/s11661-016-3568-6.

[8] B. Liu, X. Zhang, X. Zhou, T. Hashimoto, J. Wang, The corrosion behaviour of machined AA7150-T651 aluminium alloy, Corrosion Science. 126 (2017) 265–271. https://doi.org/https://doi.org/10.1016/j.corsci.2017.07.008.

[9] T. Suratwala, W. Steele, L. Wong, M.D. Feit, P.E. Miller, R. Dylla-Spears, N. Shen, R. Desjardin, Chemistry and Formation of the Beilby Layer during Polishing of Fused Silica Glass, Journal of the American Ceramic Society. 98 (2015) 2395–2402. https://doi.org/10.1111/jace.13659.

[10] D.M. Turley, L.E. Samuels, A. Vale, The Nature of Mechanically Polished Surfaces of Copper, Metallography. 18 (1985) 149–160.

[11] A.H. Advani, L.E. Murr, D. Matlock, A surface deformation region on mechanically polished surfaces of 316 stainless steels: Its effects on the sensitization of the alloy, Scripta Metallurgica et Materialia. 26 (1992) 489–494. https://doi.org/https://doi.org/10.1016/0956-716X(92)90635-R.
[12] Z. Zhao, G.S. Frankel, The effect of temper on the first breakdown in AA7075, Corrosion Science. 49 (2007) 3089–3111. https://doi.org/10.1016/j.corsci.2007.02.004.
[13] Z. Zhao, G.S. Frankel, On the first breakdown in AA7075-T6, Corrosion Science. 49 (2007) 3064–3088. https://doi.org/10.1016/j.corsci.2007.02.001.
[14] S.S. Wang, F. Yang, G.S. Frankel, Effect of altered surface layer on localized corrosion of aluminum alloy 2024, Journal of the Electrochemical Society. 164 (2017) C317–C323. https://doi.org/10.1149/2.1541706jes.
[15] S.S. Wang, J.T. Jiang, J.F. Chen, L. Zhen, J.F. Chen, G.S. Frankel, S.L. Dai, Mechanism of Localized Breakdown of 7000 Series Aluminum Alloys, Journal of the Electrochemical Society. 160 (2013) C493–C502. https://doi.org/10.1149/2.080310jes.
[16] J. Seong, F. Yang, F. Scheltens, G.S. Frankel, N. Sridhar, Influence of the Altered Surface Layer on the Corrosion of AA5083, Journal of The Electrochemical Society. 162 (2015) C209–C218. https://doi.org/10.1149/2.0321506jes.
[17] S.S. Wang, J.T. Jiang, G.H. Fan, A.M. Panindre, G.S. Frankel, L. Zhen, Accelerated precipitation and growth of phases in an Al-Zn-Mg-Cu alloy processed by surface abrasion, Acta Materialia. 131 (2017) 233–245. https://doi.org/10.1016/j.actamat.2017.03.074.
[18] S.-S. Wang, D. Huber, J.D. Poplawsky, H. Colijn, G.S. Frankel, The Subsurface Structure of Abraded Al-Zn-Mg-Cu Alloy, Materialia. (2021) 101065. https://doi.org/https://doi.org/10.1016/j.mtla.2021.101065.
[19] S.S. Wang, J.T. Jiang, G.H. Fan, G.S. Frankel, L. Zhen, Effects of long-term natural aging on the altered surface layer on an Al-Zn-Mg-Cu alloy and on corrosion properties, Electrochimica Acta. 266 (2018) 34–42. https://doi.org/10.1016/j.electacta.2018.02.001.
[20] K. Thompson, D. Lawrence, D.J. Larson, J.D. Olson, T.F. Kelly, B. Gorman, In situ site-specific specimen preparation for atom probe tomography, Ultramicroscopy. 107 (2007) 131–139. https://doi.org/10.1016/j.ultramic.2006.06.008.
[21] M. Murayama, Z. Horita, K. Hono, Microstructure of two-phase Al–1.7 at% Cu alloy deformed by equal-channel angular pressing, Acta Materialia. 49 (2001) 21–29.
[22] S. Bai, Z. Liu, X. Zhou, Y. Gu, D. Yu, Strain-induced dissolution of Cu-Mg co-clusters and dynamic recrystallization near a fatigue crack tip of an underaged Al-Cu-Mg alloy during cyclic loading at ambient temperature, Scripta Materialia. 64 (2011) 1133–1136. https://doi.org/10.1016/j.scriptamat.2011.03.012.
[23] Languillaume J., Kapelski G., Baudelet B., Cementite dissolution in heavily cold drawn pearlitic steel wires, Acta Materialia. 45 (1997) 1201–1212. https://doi.org/10.1016/j.corsci.2006.12.005.
[24] F. Vurpillot, A. Bostel, D. Blavette, Trajectory overlaps and local magnification in three-dimensional atom probe, 2000.
[25] L. Mullert, J.R. Galvele, Pitting potential of high purity binary aluminium alloys-I. Al–Cu alloys. Pitting and intergranular corrosion, Corrosion Science. 17 (1977) 179–193.
[26] I.L. Muller, J.R. Galvele, Pitting potential of high purity binary aluminium alloys-II. Al–Mg and Al–Zn alloys, Corrosion Science. 17 (1977) 995–1007. https://doi.org/10.1016/S0010-938X(77)80014-0.

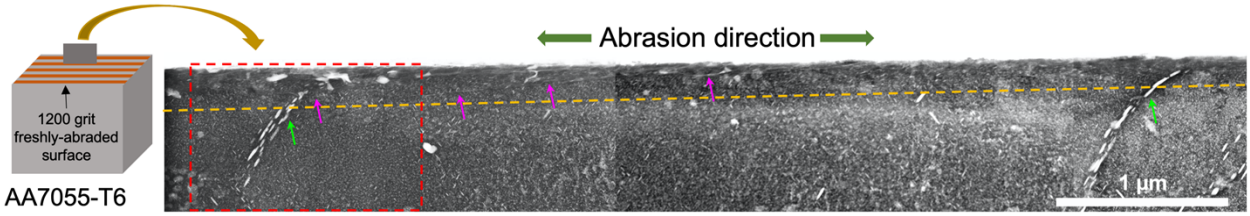

Figure 1. A collage of cross-sectional HAADF images of the subsurface microstructure in the freshly abraded AA7055-T6. The region above the orange dashed lines is the ASL. The pink arrows indicate the newly formed subgrain boundaries in the ASL. The green arrows indicate the original subgrain/grain boundaries in the underlying substrate. EDS maps shown in Figure 2 were acquired from the area marked with a rectangle.

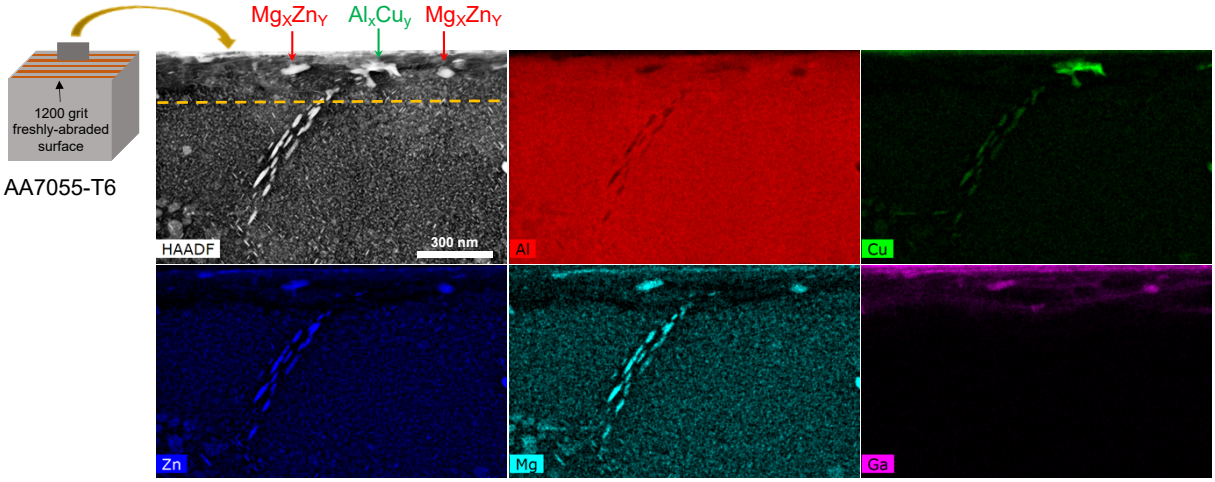

Figure 2. EDS maps of the area marked with the rectangle in Figure 1. The region above the orange dashed lines is the ASL.

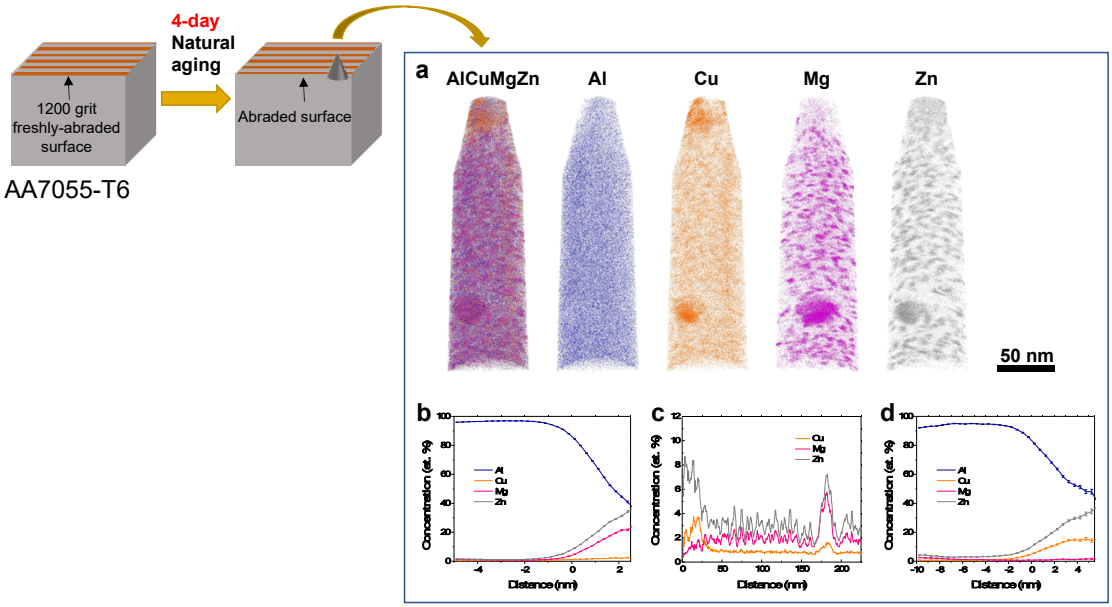

Figure 3. APT analysis of the subsurface microstructure in abraded AA7055-T6. (a) Distributions of ions in the reconstructed needle; (b) proximity histogram across the 5 at% Mg (pink) isoconcentration surface of the smaller bottom precipitates; (c) a top to bottom one dimensional concentration profile; (d) proximity histogram across the 10 at% Zn (gray) isoconcentration surface of the Zn-rich region at the top of the needle.

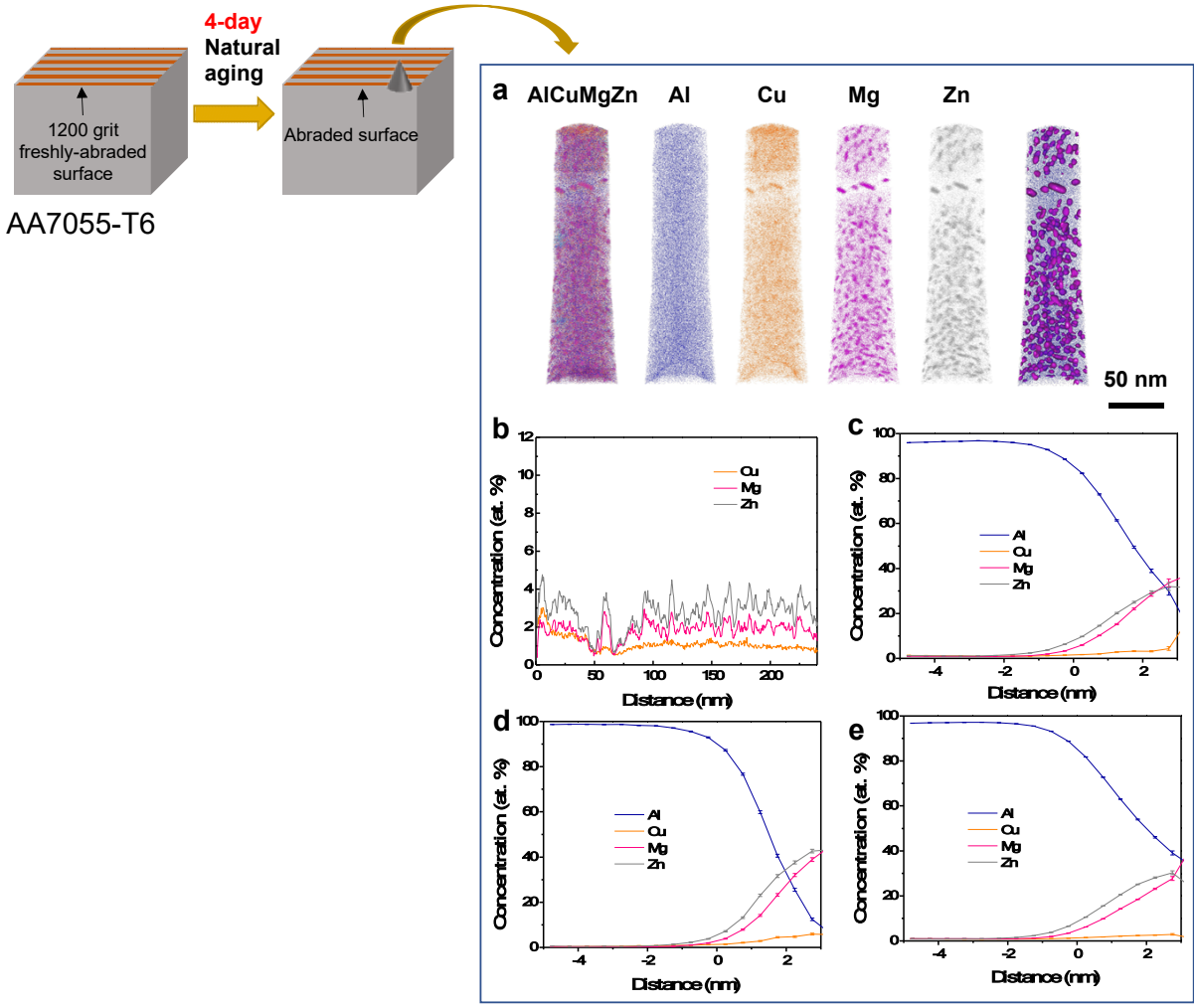

Figure 4. APT analysis of the subsurface microstructure in abraded AA7055-T6. (a) Distributions of ions in the reconstructed needle; (b) a top to bottom one dimensional concentration profile; (c,d,e) proximity histograms across the 5 at% Mg (pink) isoconcentration surfaces of the precipiates at the top, middle (larger), and bottom of the needle, respectively. All precipitates most likely have similar composition. The smaller precipitate compositions are expected to be underestimated due to artificial mixing of matrix and precipitate ions as a reuslt of APT aberrations at the precipitate/matrix interfaces.

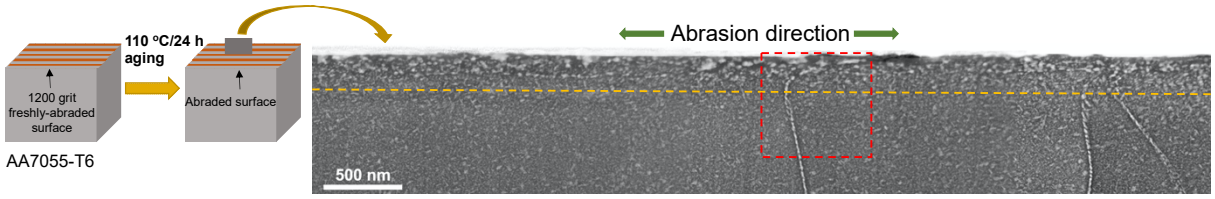

Figure 5. A collage of cross-sectional HAADF images of the subsurface microstructure in abraded and artificially aged AA7055-T6. The region above the orange dashed lines is the ASL. EDS maps shown in Figure 6 were acquired from the area marked with a rectangle.

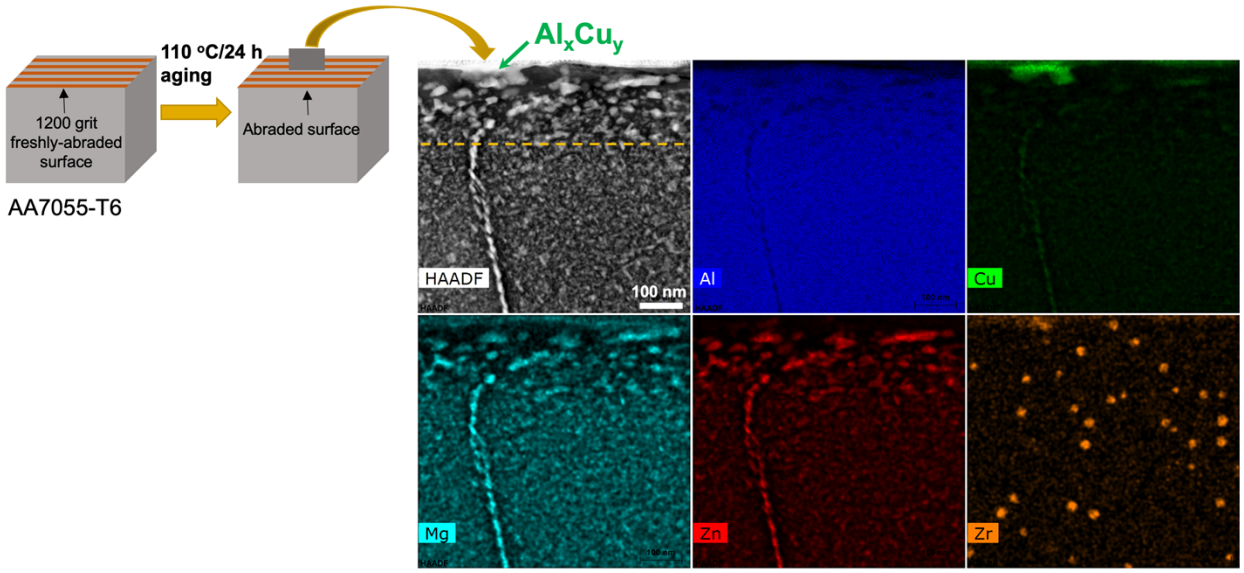

Figure 6. A HAADF image and EDS maps of the area marked with a rectangle in Figure 5.

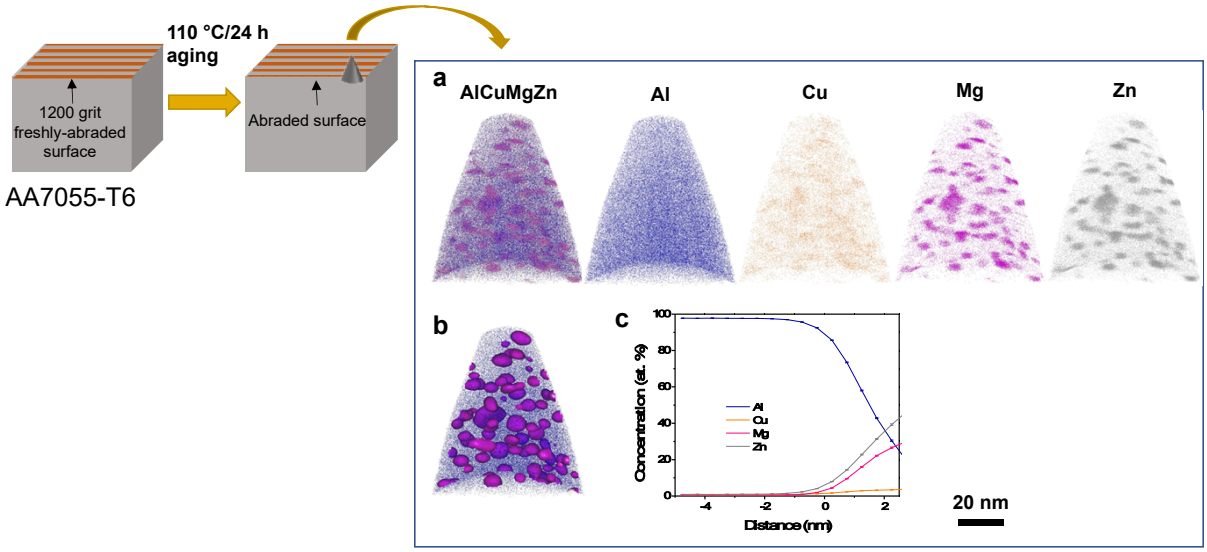

Figure 7. APT analysis of the subsurface microstructure in abraded and artificially aged AA7055-T6. (a) Distributions of ions in the reconstructed needle; (b,c) precipitates and proximity histograms across the 5 at% Mg (pink) isoconcentration surfaces of the precipiates.

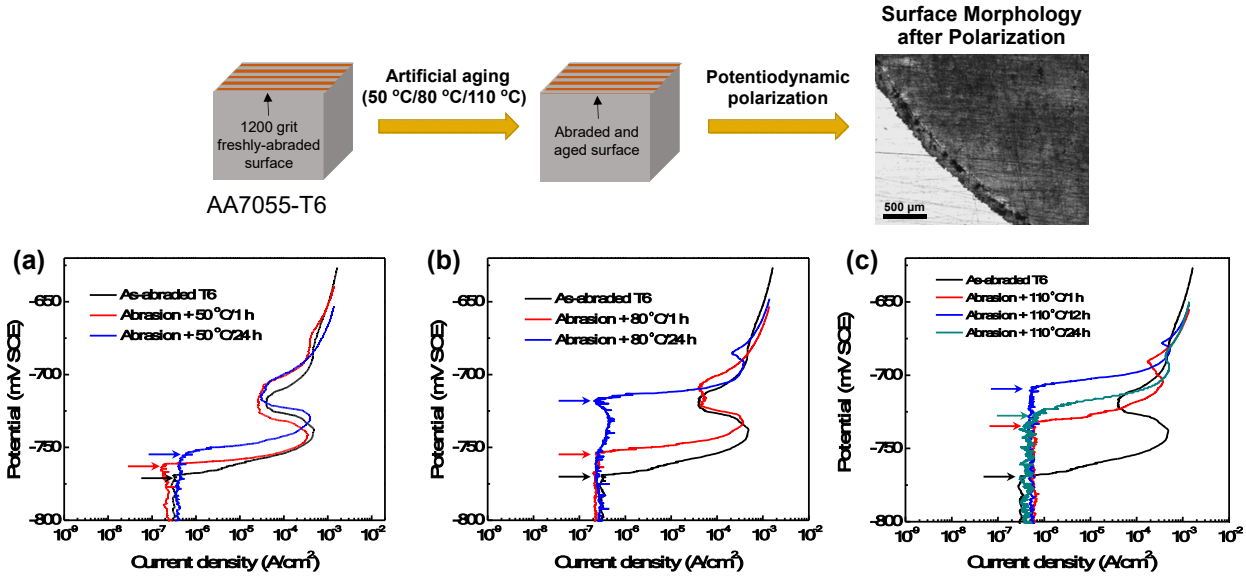

Figure 8. Anodic potentiodynamic polarization curves of 1200 grit abraded AA7055-T6 samples with different conditions in deareated 3.5 wt% NaCl solution. The arrows indicate the ASL breakdown potentials. An optical microscopy image shows the surface morphology after polarization.

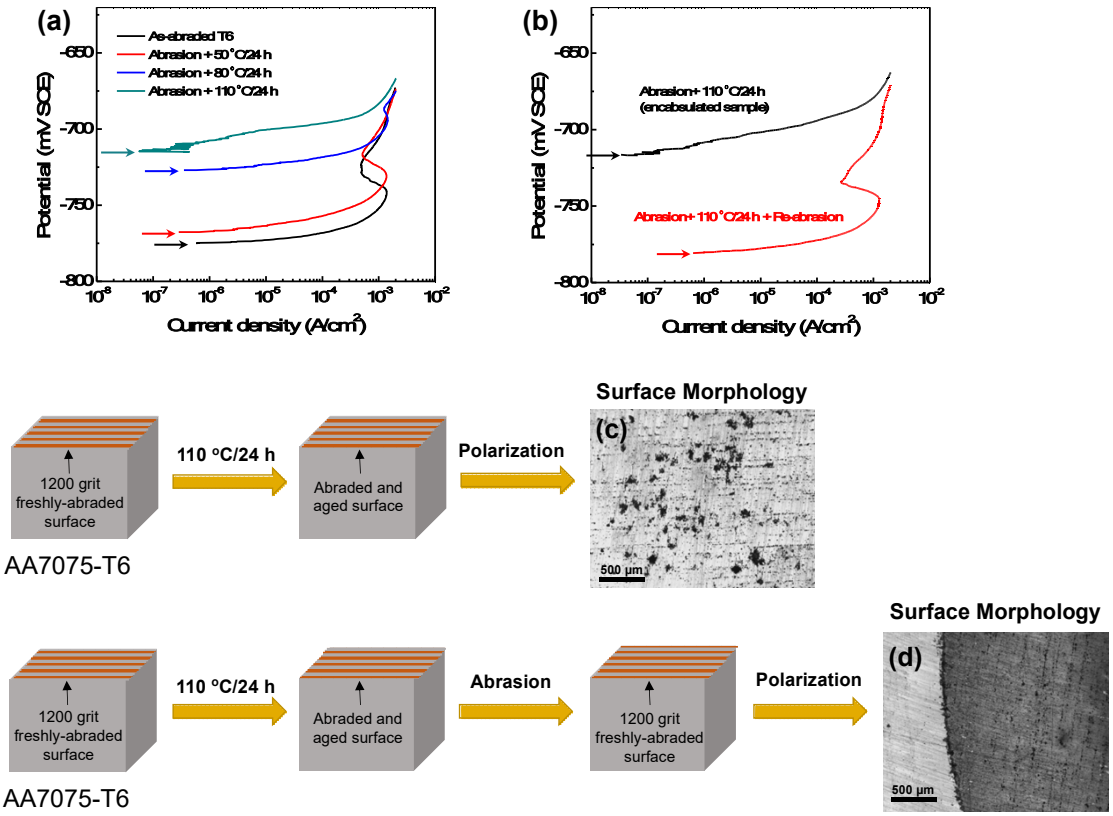

Figure 9. (a,b) Anodic potentiodynamic polarization of 1200 grit abraded AA7075-T6 samples with different conditions in air-exposed 3.5 wt% NaCl solution. The arrows indicate the ASL breakdown potentials. (c,d) Optical microscopy images show the surface morphology after polarization.